

# Decoherence dynamics across sub-Planckian to arbitrary scales using kitten states

Naeem Akhtar,<sup>1</sup> Jia-Xin Peng,<sup>2,\*</sup> Tan Hailin,<sup>3,†</sup> Xiaosen Yang,<sup>4,‡</sup> and Dong Wang<sup>1,§</sup>

<sup>1</sup>*School of Physics, Anhui University, Hefei 230601, China*

<sup>2</sup>*School of Physics and Technology, Nantong University, Nantong, 226019, China*

<sup>3</sup>*Department of Physics, Zhejiang Normal University, Jinhua 321004, China*

<sup>4</sup>*Department of Physics, Jiangsu University, Zhenjiang, Jiangsu 212013, China*

(Dated: December 18, 2025)

Environmental decoherence occurs when a quantum system interacts with its surroundings, progressively reducing quantum interference and coherence, complicating the preservation of critical quantum properties over time, especially during experimental implementation. The effect of decoherence varies depending on the phase-space features of quantum states, which are theoretically characterized by the Wigner phase space and appear at different scales. We explore the compass state and its photon-added and photon-subtracted variants, each of which exhibits phase-space features with dimensions beyond the Planck scale, making them suitable for quantum sensing applications. We investigate the interaction of these states with a heat reservoir by employing a range of well-established theoretical techniques, revealing a clear tradeoff between the degree of fineness in the smallest features, such as the sub-Planck structure, and the extent of decoherence. Specifically, increasing the parameters enhances sub-Planck precision in phase space, concomitantly amplifying the fragility of these compass states to undesired decoherence. Our general illustration, validated through these compass states, also applies to any pure quantum state interacting with the considered heat reservoir, exhibiting enhanced sustainability of features at larger phase-space extensions.

## I. INTRODUCTION

The phenomenon of interference is a crucial aspect of quantum mechanics [1, 2], capable of inducing non-classical features between the composite components of a state [3–15], which can be characterized in position–momentum phase space via the Wigner function [16–20]. Quantum interference in phase space can yield superoscillatory patterns, in which the phase-space area of a fundamental structure may surpass the typical uncertainty principle constraints [21]. This calls into question the widely held belief that phase-space features cannot be finer than the Planck scale ( $\hbar$ ), demonstrating that quantum interference can develop phase-space features at sub-Planck scales ( $\ll \hbar$ ) [22, 23]. These tiny phase-space features are critical since such fine features may lead to significant physical ramifications [24–28].

Multiphoton manipulations are crucial for advancing the nonclassical properties of quantum states [29–40]. Their compatibility with modern experimental platforms provides a practical and accessible approach for generating nonclassical states [41, 42]. The photon addition and subtraction operations applied to the standard compass states [22], for example, resulted in the formation of crucial phase-space features [43]. Decoherence is a major obstacle to preserving such quantum features [44–79], which becomes more challenging in the experimental settings [15, 41, 42, 80–88]. In other words, decoherence is stressed as a fundamental barrier to the advancement

of quantum information technologies [52], though its impact can be mitigated using a range of established techniques [89–94].

In the Wigner phase-space representation [16, 17], non-classical effects manifest as structures of differing scales, which can exhibit distinct susceptibility to environmental decoherence. This work aims to characterize the geometric variation in decoherence effects across phase-space regions, a phenomenon that remains largely unexplored. We examine two physically relevant examples exhibiting crucial sub-Planckian traits, the compass state [22] and its optimized version [43], under environmental decoherence. We employ the heat reservoir as a controlled source of decoherence [51, 95–97], which enables a simplified investigation while progressively attenuating the quantum features of the states and steering them toward classical mixtures, thus illustrating the quantum-to-classical transition. We demonstrate our results by examining the time evolution of the Wigner distributions within the corresponding reservoir.

The crucial quantum features, manifested as negative regions in the phase space [98], gradually diminish, as indicated by the attenuation of corresponding sub-Planckian traits. Optical tomogram distributions provide additional insight by precisely highlighting the degraded regions of the Wigner distributions [99–102]. We also quantify the loss of purity during thermal contact using linear entropy [97], and subsequently validate the conclusions of our adopted theoretical frameworks in relation to the phase-space-guided robustness. The impact of decoherence on nonclassical phase-space features appears to scale inversely with their volume or area; tiny features (such as sub-Planckian traits) decay more rapidly than larger ones. In other words, quantum states exhibiting minimal phase-space features at the lower scales lose

\* [JiaXinPeng@ntu.edu.cn](mailto:JiaXinPeng@ntu.edu.cn)

† [tanhai6626@outlook.com](mailto:tanhai6626@outlook.com)

‡ [yangxs@ujz.edu.cn](mailto:yangxs@ujz.edu.cn)

§ [dwang@ahu.edu.cn](mailto:dwang@ahu.edu.cn)

quantum coherence quickly, as evidenced in the presented examples.

Specifically, in our cases, either increasing the number of added photons or raising the amplitudes of the superposed coherent states results in the development of finer phase-space structures, which give rise to crucial sub-Planckian features. Although these finer-scale features enhance the capacity of the states for quantum sensing, they also increase susceptibility to decoherence. By contrast, applying photon subtraction after photon addition can produce comparatively larger-scale phase-space features, making the resulting states more stable against decoherence. Our analysis begins with a characterization of the crucial phase-space features of the compass states in Sec. II, followed by an evaluation of their robustness against decoherence using multiple theoretical frameworks in Sec. III. In Sec. IV, we develop a general framework for phase-space-scale-dependent robustness and illustrate our states as particular instances. The results are summarized in Sec. V.

## II. CRUCIAL QUANTUM FEATURES

In this section, we present compass states and their relevant precursors under investigation, specifically those obtained by applying multiphoton operations on coherent states and their superpositions. Interference (or nonclassical) phase-space patterns at the sub-Planck scale are crucial for quantum metrology [23, 43, 103–111]. The optimized compass state [43], which is the central focus of this work, exemplifies these sub-Planckian features and is now incorporated into our discussion. We focus on the key phase-space features of the optimal compass state [43], comparing them with those of the original compass state [22].

The nonclassical structures in phase space are described by the Wigner function [17], which is a tool used to represent quantum states in phase space. In other words, the Wigner function is the hallmark of nonclassicality [18–20, 112], with its marginals representing the statistics of quadrature operators [113]. Mathematically, the Wigner function for the density operator  $\hat{\rho}$  is the expectation value of the parity kernel [16, 34, 114], that is,

$$W_{\hat{\rho}}(\beta) = \text{tr}(\hat{\rho}\hat{\Delta}(\alpha)), \quad (1)$$

where

$$\hat{\Delta}(\alpha) = 2\hat{D}(\alpha)\hat{\Pi}\hat{D}^\dagger(\alpha) \text{ with } \hat{\Pi} = (-1)^{\hat{a}^\dagger\hat{a}} \quad (2)$$

denotes the displaced parity operator with  $\hat{D}(\alpha) = \exp(\alpha\hat{a}^\dagger - \alpha^*\hat{a})$ , and  $\hat{a}$  ( $\hat{a}^\dagger$ ) being the annihilation (creation) operators. The phase space of a quantum state  $\hat{\rho}$  is represented by the vector  $\beta = (x, y)^\top$ , where  $x$  and  $y$  correspond to the position and momentum coordinates, respectively [17].

### A. Key illustrations and their phase space

Photon addition and subtraction, when applied with the appropriate selection and sequencing, can yield a nonclassical variant of the coherent state  $(|\alpha\rangle)$  [43], denoted as  $|\Omega_\alpha\rangle = \hat{a}^q\hat{a}^{\dagger p}|\alpha\rangle$  with  $p$  and  $q$  representing the quantity of added and subtracted photons, respectively. The Wigner function of the coherent state  $(|\alpha\rangle)$  exhibits a Gaussian peak and serves as a classical reference, while its photon-altered counterpart can exhibit negativity in the Wigner distribution, indicating its nonclassicality [18–20, 112]. This negativity in the Wigner distribution is controlled by the multiphoton operations applied to the state.

Photon addition and subtraction applied to the compass state have resulted in an optimized version with improved phase-space characteristics [43]. The mathematical form of this optimized compass state is

$$|\bowtie\rangle = \frac{1}{\sqrt{\aleph^\bowtie}} (|X\rangle + |Y\rangle), \quad (3)$$

where  $|X\rangle = |\Omega_{\alpha_1}\rangle + |\Omega_{\alpha_2}\rangle$  specifically belongs to the photon-added and then subtracted case of the cat state aligned along the position ( $x$ ) axis in the phase space, while  $|Y\rangle = |\Omega_{\alpha_3}\rangle + |\Omega_{\alpha_4}\rangle$  represents the vertical version of the cat state, aligned along the momentum ( $y$ ) axis of the phase space. We set  $\alpha_1 = \frac{X_0}{\sqrt{2}}$ ,  $\alpha_2 = \frac{-X_0}{\sqrt{2}}$ ,  $\alpha_3 = \frac{iX_0}{\sqrt{2}}$  and  $\alpha_4 = \frac{-iX_0}{\sqrt{2}}$  with  $X_0 \in \mathbb{R}^+$ . This optimized compass state for smaller  $X_0$  values and  $p = q = 0$  leads to the well-known superposition of two kitten states.

The normalization constant  $\aleph^\bowtie$  is denoted as

$$\aleph^\bowtie = (-1)^{p+q} \sum_{i,j=1}^4 \sum_{n=0}^p \frac{(-1)^n (p!)^2}{n! [(p-n)!]^2} G_{\alpha_i, \alpha_j} \exp(\alpha_i^* \alpha_j) \times H_{p-n, q}(i\alpha_j, i\alpha_i^*) H_{p-n, q}(i\alpha_i^*, i\alpha_j) \quad (4)$$

with  $H_{p-n, q}(\cdot)$  representing the bivariate Hermite polynomial, and

$$G_{\alpha_i, \alpha_j} = \exp \left[ -\frac{1}{2} (|\alpha_i|^2 + |\alpha_j|^2) \right]. \quad (5)$$

The Wigner function of the optimized compass state  $|\bowtie\rangle$  can be obtained using Eq. (1), yielding the following compact analytical expression:

$$W_{|\bowtie\rangle}(\beta) = \frac{1}{\aleph^\bowtie} \left( \sum_{i=1}^4 W_{|\bowtie_i\rangle} \langle \bowtie_i |(\beta) + \sum_{i \neq j=1}^4 W_{|\bowtie_i\rangle \langle \bowtie_j |}(\beta) \right) \quad (6)$$

with different effects in the phase space.

The first terms of Eq. (6) represents the superposed components of the states, while the second term corresponds to the nonclassical effects associated with these

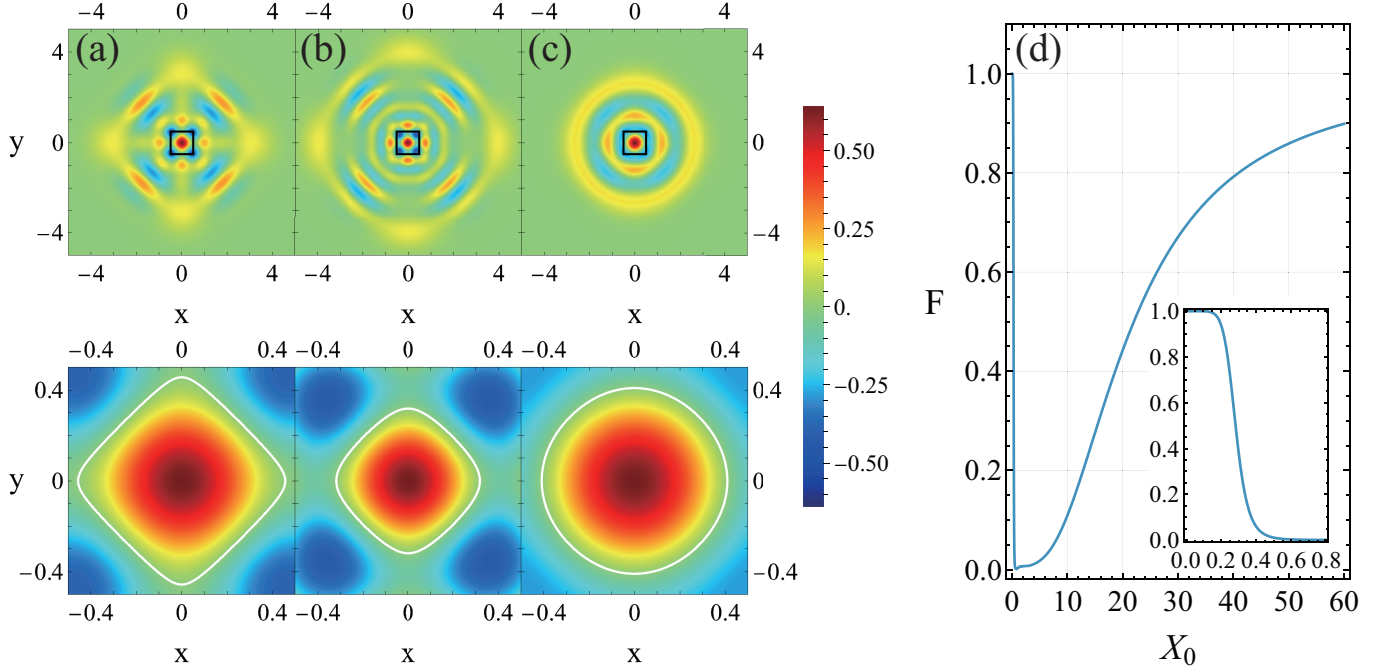


FIG. 1. The Wigner distributions  $W_{|<|>}(\beta)$ , with  $\beta = \frac{(x+iy)}{\sqrt{2}}$ : (a)  $p = q = 0$  and  $X_0 = 3$ ; (b)  $p = q = 14$  and  $X_0 = 1.5$ ; (c)  $p = q = 14$  and  $X_0 = 0.5$ . The black box in (a)–(c) marks the focused phase-space region, shown also across each main figure. The white contours represent regions where the Wigner distributions have virtually zero amplitudes near the origin. (d) The overlap  $F = |\langle C | <| \rangle|^2$  between the compass state  $|C\rangle$  and its optimized version  $|<|>$  in the case of  $p = q = 14$ .

superposed components, where

$$W_{|<|>}(\beta) = W_{|\alpha_i\rangle\langle\alpha_j|}(\beta) \sum_{n=0}^p \frac{(-1)^n (p!)^2}{n![(p-n)!]^2} \times H_{p-n,q} \left( i\gamma_j^*, i\alpha_i \right) H_{p-n,q} \left( -i\gamma_i, -i\alpha_j^* \right) \quad (7)$$

with

$$\gamma_k = 2\beta - \alpha_k \quad (8)$$

and

$$W_{|\alpha_i\rangle\langle\alpha_j|}(\beta) = G_{\alpha_i, \alpha_j} \exp \left[ -\alpha_i \alpha_j^* - 2(|\beta|^2 - \alpha_j^* \beta) - \alpha_i \beta^* \right]. \quad (9)$$

Figure 1 depicts heat maps of the Wigner functions of the compass state and its optimized variant, illustrating the variations in associated phase-space features by varying the parameters  $X_0$ ,  $p$ , and  $q$ . The central region emphasized in the black box [panels (a)–(c) of Fig. 1] represents the central sub-Planck structure, as also separately illustrated for each case, with white contours representing the zeros of the Wigner distribution around the phase-space

origin. These contours highlight the borders of the fundamental sub-Planck structure and aid in distinguishing between its isotropic and anisotropic forms.

The original compass state arises when  $p = q = 0$  and  $X_0$  is sufficiently greater, as illustrated by Fig. 1(a), and theoretically is the superposition of four coherent states [22],

$$|C\rangle = \frac{1}{\sqrt{N_c}} \left[ \left| \frac{X_0}{\sqrt{2}} \right\rangle + \left| \frac{-X_0}{\sqrt{2}} \right\rangle + \left| \frac{iX_0}{\sqrt{2}} \right\rangle + \left| \frac{-iX_0}{\sqrt{2}} \right\rangle \right], \quad (10)$$

where the normalization coefficient ( $N_c$ ) can be obtained by setting  $p = q = 0$  in Eq. (4). As shown in Fig. 1(a), the central sub-Planck structure of the compass state is confined within an anisotropic region (a tilelike pattern), clearly demonstrating its directional asymmetry.

Nonzero values of  $p$  and  $q$  combined with a relatively small  $X_0$  give rise to an optimized version of the compass state, in which variations in  $X_0$  modify the central sub-Planck structure. Figure 1(b) shows the case with  $p = q = 14$  and a relatively smaller  $X_0$ , resulting in an optimized compass state that exhibits similar phase-space characteristics to those in Fig. 1(a), including a central anisotropic sub-Planck structure. Note that for the comparatively smaller  $X_0$  and  $p = q = 0$ , the

optimized compass state simply results in the superposition of two kitten states that lack sub-Planck structures [43]. This shows that reported sub-Planck-scale features in Fig. 1(b) are solely due to the multiphoton operations [43].

A further decrease in the value of  $X_0$ , while keeping the same  $p$  and  $q$  values as in Fig. 1(b), results in the optimized compass state displaying an isotropic sub-Planck structure, as shown in Fig. 1(c). This isotropy is characterized by the confinement of the feature within a circular region. This isotropic form is a superior manifestation of sub-Planck traits, as it enables uniform sensitivity enhancement to phase-space displacements in all directions [43, 115]. Notably, the optimized compass state considered here was overlooked in earlier work [43] regarding its refined phase-space features, in contrast to states produced by reversing photon operations (e.g., subtraction followed by addition), where such sub-Planckian refinement was not clearly demonstrated. We demonstrate that an appropriate choice of the coherent-state amplitudes in the superposition can likewise produce isotropic sub-Planckian structures.

The transition between the compass state and its optimized counterpart is solely determined by the choice of parameters  $X_0$ ,  $p$ , and  $q$ . Smaller values of the parameter  $X_0$  provide a higher distinguishability between the compass state and its optimized version, as evident in Fig. 1(d), where we plot the overlap  $F(X_0) = |\langle C | \times \rangle|^2$ , which quantitatively compares the compass state with its multiphoton-altered version. This shows that the photon addition followed by subtraction significantly affects the state with a particular choice of  $X_0$ . For smaller values of  $X_0$ , the optimized version of the compass state differs notably from the original compass state, as also confirmed by their Wigner distributions, and in these situations the photon operations applied are highly effective in deforming the state. However, as the parameter  $X_0$  increases, the effectiveness of photon operations diminishes, and at relatively large  $X_0$  values, the optimized compass state gradually converges toward its original form [22].

## B. Sub-Planckness and Wigner negativity

For the optimized compass state [43], specific choices of photon addition and subtraction have a pronounced effect on the critical sub-Planckian features. Increasing the number of added photons generally compresses the core sub-Planck structures, enhancing their resolution, whereas photon subtraction following the photon addition tends to enlarge these structures, thereby reducing their sub-Planck character [43]. In certain cases, particular combinations of these operations can also produce isotropic sub-Planck structures.

We now further emphasize the impact of multiphoton operations on the nonclassical characteristics of the optimized compass state by evaluating its Wigner negativ-

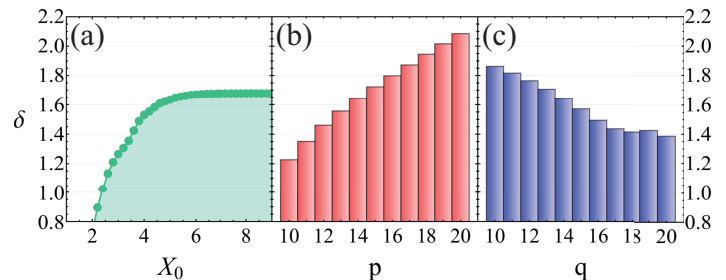


FIG. 2. Variation of negativity in the Wigner function  $W_{|x\rangle}(\beta)$ : (a)  $p = q = 0$ , (b)  $q = 14$ ,  $X_0 = 1.5$ , and (c)  $p = 14$ , with  $X_0 = 1.5$ .

ity [112]

$$\delta = \iint |W_{\hat{\rho}}(x, y)| dx dy - 1. \quad (11)$$

When the Wigner function  $W_{\hat{\rho}}$  is non-negative, the quantity  $\delta$  is equal to zero. This is evident in the case of coherent states and squeezed vacuum states, where  $\delta = 0$  [112]. Since squeezed vacuum states are recognized as nonclassical, this suggests that the parameter ( $\delta$ ) alone may not be sufficient to fully characterize nonclassicality in all cases. However, the presence of negativity in the Wigner function offers enough evidence of nonclassicality in a state [18–20, 112].

We numerically calculate Eq. (11) for our examples and illustrate them in Fig. 2 for various parameter selections. Figure 2(a) shows the case of the compass state ( $p = q = 0$ ), where we plot Wigner negativity ( $\delta$ ) over a few  $X_0$  values, which shows that the negative volume of the associated Wigner function increases as the amplitude of coherent states  $X_0$  rises, up to a certain point, beyond which the negativity becomes constant and remains invariant for further increases in  $X_0$ . Figures 2(b) and 2(c) show the Wigner negativity of the optimized compass state for a fixed  $X_0$ , while the number of added photons ( $p$ ) and subtracted photons ( $q$ ) are varied. This demonstrates that, with an appropriate choice of order and application, photon addition ( $p$ ) enhances the Wigner negativity of the optimized compass state, whereas photon subtraction ( $q$ ) reduces it [43].

## III. NOTORIOUS DECOHERENCE

As discussed in Sec. II, the crucial phase-space features of the standard compass state and its variant are influenced by different parameters, with the standard compass state representing a limiting case of the optimized one; that is, by adjusting certain parameters, these two states can be easily transformed into each other. This section now examines how the effect of decoherence varies during the transition between these two states by analyzing their interaction with a thermal reservoir [49, 58].

The master equation governing the temporal evolution of a single-mode state  $\hat{\rho}$  in the presence of the considered thermal reservoir is given by:

$$\begin{aligned}\dot{\hat{\rho}} = & (\bar{n} + 1)(2\hat{a}\hat{\rho}\hat{a}^\dagger - \hat{a}^\dagger\hat{a}\hat{\rho} - \hat{\rho}\hat{a}^\dagger\hat{a}) \\ & + \omega\bar{n}(2\hat{a}^\dagger\hat{\rho}\hat{a} - \hat{a}\hat{a}^\dagger\hat{\rho} - \hat{\rho}\hat{a}\hat{a}^\dagger),\end{aligned}\quad (12)$$

where the first term represents the transfer through the decay of photons from the quantum system to the thermal reservoir, and the second term corresponds to the transfer of excitation from the non-zero temperature heat reservoir to the quantum system. The field decay rate is labeled by  $\omega$ , and the average thermal photon number in the cavity is  $\bar{n}$ . When  $\bar{n} = 0$ , Eq. (12) depicts a zero-temperature reservoir, which is also known as the photon-loss reservoir [116].

In this section, we mainly analyze the impact of decoherence on the crucial phase-space features of the compass state and its optimal version introduced in Sec. II A, employing a range of theoretical methods. The discussion is detailed in the following sections. Sec. III A examines the time evolution of the Wigner distributions, while Sec. III B analyzes the tomogram distributions of the considered compass states. The stability of the crucial sub-Planck structures under decoherence is investigated in Sec. III C, and the temporal evolution of the resulting Wigner negativity is discussed in Sec. III D. Finally, Sec. III E presents the time evolution of the linear entropy.

### A. Damping of interference fringes

This section focuses on the temporal evolution of the Wigner function of the optimized compass state [Eq. (3)] under the influence of the thermal reservoir described by Eq. (12), considering a range of parameter settings. The standard compass state is treated as a special case within the general framework of the optimized compass state. The temporal evolution of the Wigner distribution associated with the optimized compass state under the influence of the reservoir is computed using [117]

$$W_{\hat{\rho}}(\eta, t) = \frac{2}{\bar{T}} \int \frac{d^2\beta}{\pi} W_{\hat{\rho}}(\beta) \exp \left[ \frac{-2|\eta - \beta e^{-\omega t}|^2}{\bar{T}} \right], \quad (13)$$

where  $\eta = \frac{(x+iy)}{\sqrt{2}}$  and  $\bar{T} = (1+2\bar{n})T$ , with  $T = 1 - e^{-2\omega t}$ .

Since the optimal compass state is constructed by employing the sequence of annihilation and creation operators on the standard, which in this case are in the antinormal order ( $\hat{a}$  is placed before  $\hat{a}^\dagger$ ), which makes the calculations leading to the temporal evolution of the resulting Wigner functions highly complicated, and using the identities provided in the Ref. [118] can be used to rewrite these bosonic operators written in their normal order as  $\hat{a}^n\hat{a}^{\dagger m} = (-i)^{n+m} : H_{n,m}(i\hat{a}^\dagger, a) :$ , where the presence of the bivariate Hermite polynomial

$H_{n,m}$  in the integral still complicates the calculation. However, by transforming the Hermite polynomial using the generating function from Ref. [119],  $H_{m,n}(x_1, y_1) = \frac{\partial^{n+m}}{\partial s^n \partial m^m} e^{-st+sx_1+ty_1} \Big|_{s,t=0}$  makes it comparatively easier to solve.

We also make frequent use of the identity  $\exp(Cs + Dt + Est) = \sum_{l=0}^{\infty} \frac{E^l}{l!} \frac{\partial^{2l}}{\partial C^l \partial D^l} [\exp(Cs + Dt)]$  in our calculations, and we find the following integral formula quite useful in our derivations [120]

$$\begin{aligned}\int_{-\infty}^{\infty} d^2\beta \exp \left[ A|\beta|^2 + B\beta + C\beta^* + D\beta^2 + K\beta^{*2} \right] \\ = \frac{\pi}{\sqrt{A^2 - 4DK}} \exp \left[ \frac{-ABC + B^2K + C^2D}{A^2 - 4DK} \right],\end{aligned}\quad (14)$$

whose convergent conditions are  $\text{Re}[A \pm D \pm K] < 0$  and  $\text{Re} \left[ \frac{(A^2 - 4DK)}{A \pm D \pm K} \right] < 0$ .

Finally, the temporal evolution of the Wigner function belonging to the optimal compass state in the designated heat reservoir is expressed in the following compact mathematical form:

$$W_{|\times\rangle}(\eta, \tau) = \frac{1}{N^{\times}} \left[ I_{\text{coh}}(\eta, \tau) + I_{\text{int}}(\eta, \tau) \right] \quad (15)$$

with  $I_{\text{coh}}(\eta, \tau) = \sum_{i=1}^4 W_{|\times_i\rangle\langle \times_i|}(\eta, \tau)$  and  $I_{\text{int}}(\eta, \tau) = \sum_{i \neq j=1}^4 W_{|\times_i\rangle\langle \times_j|}(\eta, \tau)$ , where

$$\begin{aligned}W_{|\times_i\rangle\langle \times_j|}(\eta, \tau) := & \frac{2 \exp \left[ A - \frac{2|\eta|^2}{\bar{T}} - \alpha_i \alpha_j^* \right] G_{\alpha_i, \alpha_j}}{(k_3 + 2)\bar{T}} \\ & \times \sum_{n=0}^p \sum_{n'=0}^{\infty} \frac{(-1)^n (p!)^2 (E)^{n'}}{n! n'! [(p - n - n')!]^2} \\ & \times H_{p-n-n', q}[\Gamma_j, i\alpha_i] H_{p-n-n', q}[\Gamma_i, -i\alpha_j]\end{aligned}\quad (16)$$

with

$$E = \frac{4}{(2+k_3)}, A = \frac{(k_1 + 2\alpha_i)(k_2 + 2\alpha_j^*)}{(2+k_3)}, \quad (17)$$

$$\Gamma_j = \frac{2i(k_2 + 2\alpha_j^*)}{(2+k_3)} - i\alpha_j^*, \quad \Gamma_i = \frac{-2i(k_1 + 2\alpha_i)}{(2+k_3)} + i\alpha_i, \quad (18)$$

where  $k_1 = \frac{2e^{-\tau}\eta}{\bar{T}}$ ,  $k_2 = \frac{2e^{-\tau}\eta^*}{\bar{T}}$  and  $k_3 = \frac{2e^{-2\tau}}{\bar{T}}$ . The dimensionless version of the time  $\tau = \omega t$  is used.

The time evolution of the Wigner function associating the optimized compass state, as provided in Eq. (15), is now analyzed under the influence of the heat reservoir by varying the time parameter  $\tau$ , while keeping the average thermal photon number  $\bar{n}$  fixed and tuning other relevant parameters. We begin with the case where  $p = q = 0$  and  $X_0 = 3$ , which simply corresponds to the standard compass state [22], and the temporal evolution of the associated Wigner function under the influence of the heat reservoir is shown in Figs. 3(a)–3(c) for different

values of the time parameter  $\tau$ . Specifically, Fig. 3(a) illustrates the case at a relatively short time ( $\tau = 0.06$ ), indicating that even after such a brief interaction with the heat reservoir, the compass state has lost a substantial amount of its nonclassical features.

The degradation of nonclassical features is clearly evident, with the white contour indicating the regions where the Wigner distribution has been degraded. This highlights that the central sub-Planck features quickly blur due to decoherence, illustrating the negative impact of decoherence on the crucial features of the state. Figure 3(b) indicates that a longer interaction with the heat reservoir ( $\tau = 0.12$ ) leads to further degradation of the nonclassical phase-space features of the state. As illustrated in Fig. 3(c), when the interaction becomes significantly longer ( $\tau = 10$ ), the nonclassical features of the state are completely lost, and the Wigner function emerges as a Gaussian lobe. When the amplitude  $X_0$  is reduced, multiphoton operations become significantly more effective, resulting in the formation of optimized compass states. In the illustrated cases [Figs. 3(d)-3(f)], we uniformly set  $p = q = 14$  and  $X_0 = 1.5$ , and the analysis is carried out over different time intervals:  $\tau = 0.06$  in Fig. 3(d),  $\tau = 0.12$  in Fig. 3(e), and  $\tau = 10$  in Fig. 3(f). As the time  $\tau$  rises, the optimized compass state progressively loses its nonclassical characteristics, where the faded regions are indicated by the white contours.

For sufficiently large values of  $\tau$ , the Wigner distribution transforms into a Gaussian lobe, resembling that of the standard compass state. This indicates that at higher  $\tau$ , these states transition into a thermal state, characterized by the Wigner function ( $W_{\text{th}}(\eta) = [\pi(2\bar{n} + 1)]^{-1} \exp\left[-\frac{2|\eta|^2}{2\bar{n}+1}\right]$ ). This indicates a quantum-to-classical transition, where the system reaches thermal equilibrium, and the Wigner function of the resulting thermal state is solely influenced by the average thermal photon number  $\bar{n}$ , reducing to the vacuum state when  $\bar{n} = 0$ .

## B. Distorted tomogram distributions

The temporal evolution of the Wigner distributions evidenced that the interaction of our compass states with the heat reservoir has decreased associated nonclassical characteristics. In this section, the corresponding tomogram distribution highlights this degradation more apparently.

The quadrature histograms (tomogram function), denoted as  $R(x_\theta)$ , may also referred as marginal distributions, are the projections (Radon transformation) of the Wigner function  $W$  [99], that is,

$$R(x_\theta) = \int dy_\theta W(x_\theta \cos \theta - y_\theta \sin \theta, x_\theta \sin \theta + y_\theta \cos \theta). \quad (19)$$

The inverse Radon transform can be employed to reconstruct the Wigner function from these histograms

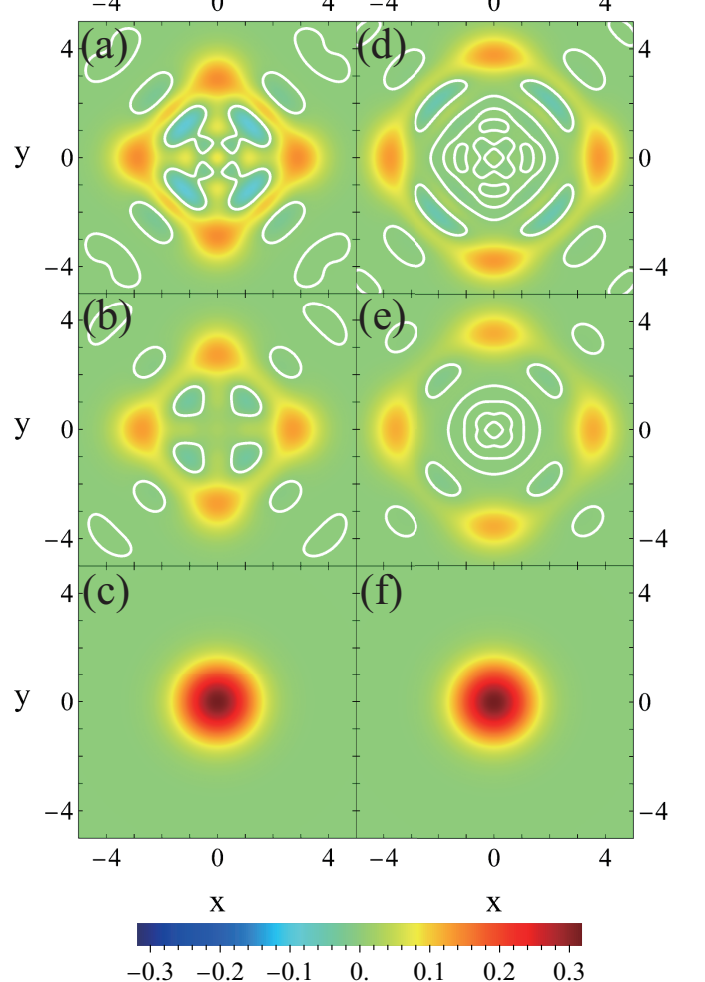


FIG. 3. The evolution over time of the Wigner functions corresponding to the compass states. The white contour highlights the regions of the Wigner distribution that have substantially decayed, ultimately evolving toward a Gaussian lobe over time. The left column represents the cases when  $p = q = 0$ ,  $X_0 = 3$ , and the right column belongs to  $p = q = 14$ ,  $X_0 = 1.5$ , each evaluated at multiple values of  $\tau$ . (a)  $\tau = 0.06$ , (b)  $\tau = 0.12$ , (c)  $\tau = 10$ , (d)  $\tau = 0.06$ , (e)  $\tau = 0.12$ , and (f)  $\tau = 10$ . In all cases, we set  $\bar{n} = 0.5$ .

$R(x_\theta)$  [101]. Note that in Eq. (19)  $\theta$  corresponds to different directions in the position-momentum phase space. We numerically computed Eq. (19) for our optimized compass state [Eq. (3)] and investigated multiple scenarios under different parameter choices, which we now explain.

First, consider the tomogram distribution ( $R$ ) for  $p = q = 0$  and  $X_0 = 3$ , simply leading to the standard compass state [22]. This case is illustrated in Fig. 4 for different values of  $\theta$  and  $\tau$ , where  $\theta = 0$  corresponds to the  $x$  direction in phase space, with the tomograms shown in Figs. 4(a)-4(c) associating with different values of  $\tau$ . Figure 4(a) shows the case when  $\tau = 0$ , representing

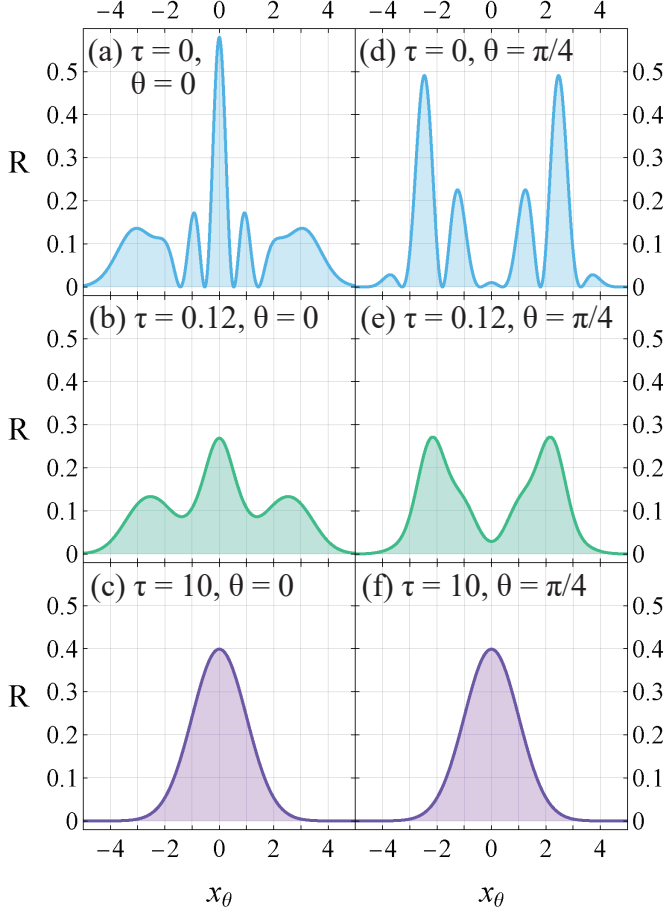


FIG. 4. Tomogram function for the case when  $p = q = 0$  and  $X_0 = 3$ , illustrating the compass state.

the non-deformed form of the marginal distribution of the standard compass state along the  $x$  direction, the oscillatory pattern around the origin mirrors the central interference pattern. When the interaction between the compass state and the heat reservoir is significant, the marginal distribution is distorted due to decoherence, as clearly observed in Figs. 4(b) and 4(c) for  $\tau = 0.12$  and  $\tau = 10$ , respectively. For a sufficiently large value of  $\tau$  the Gaussian peak as shown in Fig. 4(c) evidence that the compass state has been transformed into a thermal state.  $\theta = \frac{\pi}{4}$  represents diagonal direction in the phase space, which is observed for  $\tau = 0$ ,  $\tau = 0.12$  and  $\tau = 10$ , and is illustrated in Figs. 4(d), 4(e) and 4(f), respectively. The deformation in these marginals is pronounced as the time  $\tau$  increases, where for comparatively significant values of  $\tau$ , as observed in Fig. 4(e) corresponding marginal distribution is modified entirely compared to the prior case of Fig. 4(d), and then for sufficiently large values of  $\tau$ , as depicted in Fig. 4(f), a Gaussian peak emerges, reflecting the thermal state.

We now discuss the cases of the optimized compass state. Figure 5 represents the quadrature histograms ( $R$ ) for the case when  $p = q = 14$  and  $X_0 = 1.5$ , illustrated in

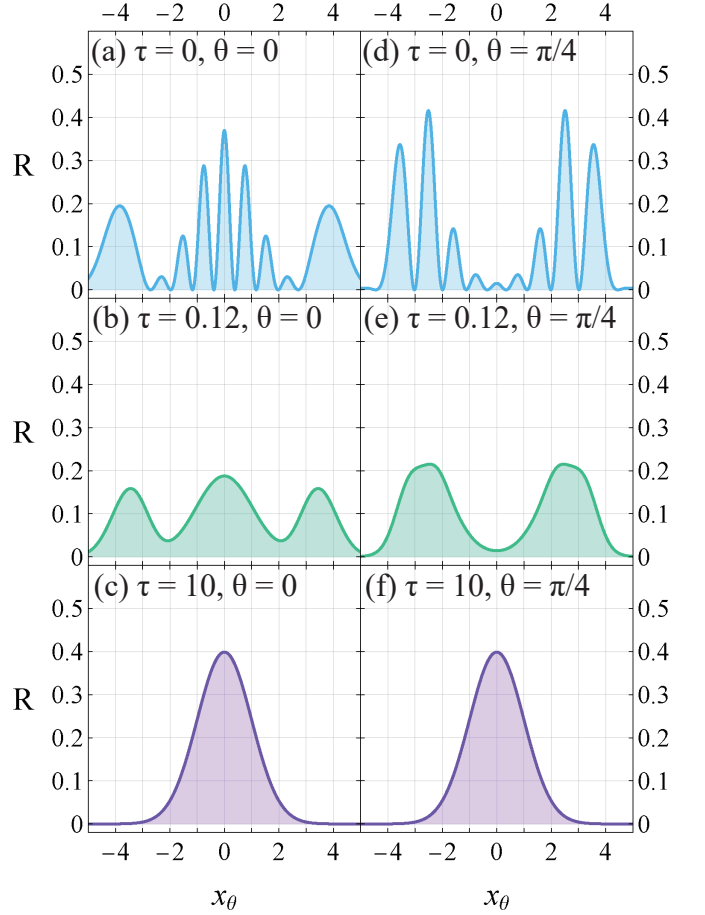


FIG. 5. Tomogram function for the case when  $p = q = 14$  and  $X_0 = 1.5$ , illustrating the optimized compass state.

different phase-space directions by varying the angle  $\theta$ ; specifically,  $\theta = 0$  corresponds to the  $x$  direction in phase space and is further examined in Figs. 5(a)–5(c) for different values of  $\tau$ . Figure 5(a) represents the situation when  $\tau = 0$  denoting the non-distorted version of the marginal distribution. As time evolves, the associated marginal distribution becomes increasingly distorted. For example, at  $\tau = 0.12$  [Fig. 5(b)], the distribution is notably altered from its initial shape. Eventually, at a much higher time ( $\tau = 10$ ), as shown in Fig. 5(c), it fully transforms into a Gaussian profile.

We now expand our observations along the  $\frac{\pi}{4}$  direction in the phase space, as illustrated in Figs. 5(d)–5(f), the increment in the values of  $\tau$  has modified the associated marginal distributions. Initially, at  $\tau = 0$ , shown in Fig. 5(d), the marginal distribution takes its original form. As time progresses, the distribution begins to deform; for example, at  $\tau = 0.12$ , depicted in Fig. 5(e), the marginal distribution shows significant distortion. At sufficiently larger values of  $\tau$ , as shown in Fig. 5(f), a Gaussian peak emerges, marking the complete loss of associated quantum signatures.

In summary, thermal decoherence has diminished the

critical nonclassical features of both the compass state and its optimized version. This loss is well apparent in the Wigner distributions, where Gaussian lobes emerge in phase space, and similarly reflected in the tomogram functions. The growing prominence of Gaussian peaks in these distributions is the message of the gradual transition from the quantum compass state to a thermal state.

### C. Fragility of sub-Planckness

In this section, we investigate the impact of decoherence on the central sub-Planck structures of the outlined compass states. We examine the effects of key parameters, such as photon addition  $p$ , photon subtraction  $q$ , amplitude  $X_0$ , and the average number of thermal photons  $\bar{n}$ , on the prominence of these crucial features using the following expression:

$$d(\tau) = \frac{W_{|k\rangle}(0, \tau)}{|W_{|k\rangle}(0, 0)|}, \quad (20)$$

and using this equation, multiple scenarios relating to our quantum compass states are depicted in Fig. 6. In each of these depicted situations, a consistent pattern develops in the associated plots. The central sub-Planck structure diminishes gradually, and a new central peak emerges. This transition from the decay to the rebuilding of the central peak, with a clear distinction between the two phases, shows the degradation of quantum states as they shift from their quantum nature to a classical regime. The curve eventually levels off, signaling the complete decay of the core sub-Planck structure and the emergence of a new central feature.

The rate at which the central sub-Planck structure deforms into a new phase-space feature is controlled by different associated parameters. This deformation is particularly noticeable in the shorter time frames, as shown in the inset of each case illustrated in Fig. 6. In Fig. 6(a), we explore scenarios where  $p = q = 0$  (compass state) and analyze the effects of varying the parameters  $X_0$  and  $\bar{n}$ . By comparing the blue and red curves in the inset of Fig. 6(a), it is observed that the central sub-Planck peak associating the compass state decays more quickly when the amplitude parameter  $X_0$  grows. Similarly, the central peak decays faster with increasing average thermal photon number ( $\bar{n}$ ) in the reservoir, as shown by the comparison of the red and black curves in the inset of Fig. 6(a).

We now explore the scenario where the parameter  $X_0$  is held constant while  $p$  and  $q$  varies (optimized compass state), as illustrated in Fig. 6(b). First, when  $p$  is changed while keeping other parameters constant, as clearly illustrated in the inset of Fig. 6(b), the red curve falls more quickly than that of the orange curve, showing that larger photon addition may cause a rise in the decoherence effect. As the number of photon subtractions  $q$  increases, as illustrated in the corresponding curves (compare the red and black curves) in the inset of Fig. 6(b), the black

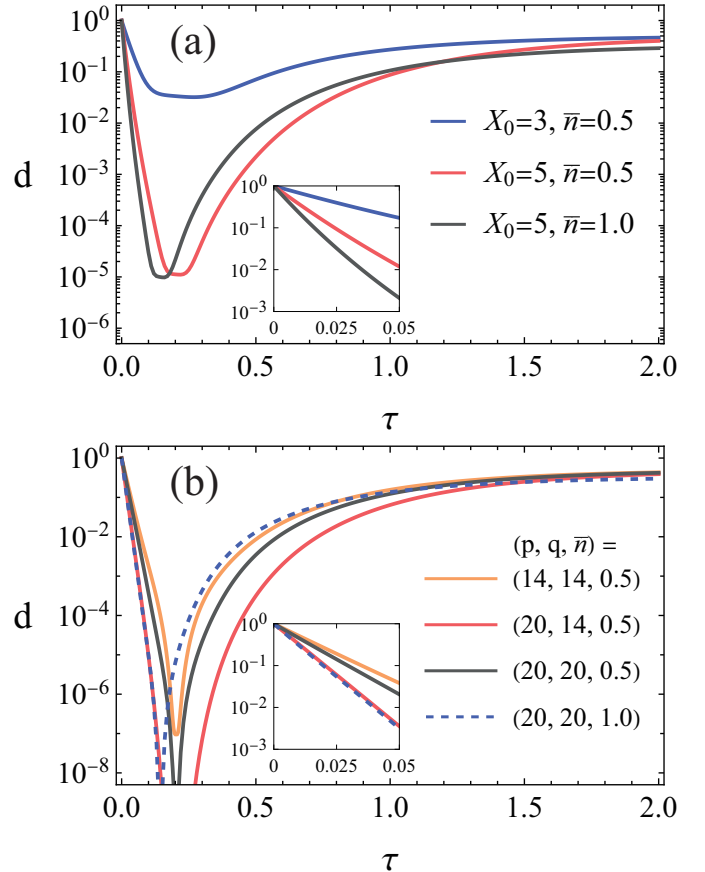


FIG. 6. The parametric function  $d$  illustrates fluctuations in the height of the central phase-space features of the compass states under decoherence: (a)  $p = q = 0$ , and (b)  $X_0 = 1.5$ .

curve, which corresponds to a higher number of photon subtractions, decays more slowly than the red curve. This suggests that increasing the number of photon subtractions can help to stabilize the sub-Planck structures against decoherence. We further observe that larger average thermal photons  $\bar{n}$  lead to increased decoherence effects on the sub-Planck structures of the optimized compass state, as observed by comparing the black and dotted blue curves of the inset shown within Fig. 6(b).

### D. Suppression of Wigner negativity

Thermal decoherence from the heat reservoir causes the nonclassical interference fringes to disappear from the phase space of our compass states, as evidenced by the reduction of negative amplitudes of the associated Wigner distributions. Over time, this process transforms the Wigner function into a positively peaked distribution, indicating the transition of the quantum state into a classical one. This transition is clearly reflected in the temporal evolution of both the Wigner distribution and the tomogram functions discussed in the previous section.

The decay of nonclassical features in the states can be

further investigated by analyzing the temporal evolution of Wigner negativity. In our study, the temporal evolution of Wigner negativity is numerically evaluated by employing

$$\tilde{\delta}(\tau) = \iint |W_{|\times\rangle}(x, y; \tau)| dx dy - 1, \quad (21)$$

and whose graphical illustration is provided in Fig. 7, evidencing the decay of the Wigner negativity over time with variations of involved parameters.

Figure 7(a) depicts the temporal evolution of the Wigner negativity of the standard compass state ( $p = q = 0$ ) by varying  $X_0$  and  $\bar{n}$ . The blue and red curves show that increasing  $X_0$  causes a greater loss of negativity in the Wigner function. Moreover, the increase in the average thermal photon  $\bar{n}$ , as shown by the red and black curve in Fig. 7(a), demonstrates that the negativity in the Wigner function decreases quickly with higher values of  $\bar{n}$ .

Figure 7(b) illustrates the impact of decoherence on the optimal compass state by changing the number of photons added ( $p$ ) and subtracted ( $q$ ), and by utilizing varied quantities of thermal photons  $\bar{n}$ , while keeping the amplitude  $X_0$  constant. As depicted by the transition from the orange to the red curve via increasing  $p$ , and from the red to the black curve by varying  $q$ , along with the change from the black to the blue curve for different values of  $\bar{n}$ , the following trends emerge: Higher photon addition  $p$  accelerates the loss of Wigner negativity, while photon subtraction  $q$  helps preserve it in our adopted cases. Same as in the previous case of the compass state, an increase in the average thermal photon  $\bar{n}$  leads to a greater loss of Wigner negativity corresponding to the optimized compass state.

### E. Loss of quantum purity

The loss of quantum features from the phase space associated with the compass states, resulting from interaction with the heat reservoir and their eventual transition into a thermal state, can be confirmed by the degradation of their purity, as discussed in this section. The purity sustained by a quantum state  $\hat{\rho}(\tau)$  over time  $\tau$  can be assessed using  $\text{tr}\hat{\rho}^2(\tau)$ . This enables the classification of pure states with  $\text{tr}\hat{\rho}^2(\tau) = 1$  and mixed states with  $\frac{1}{N} \leq \text{tr}\hat{\rho}^2(\tau) < 1$ , where  $N$  is the dimension of the density operator.

Alternatively, the linear entropy, which quantifies the mixedness (or purity), is defined as  $S(\tau) = 1 - \text{tr}[\hat{\rho}^2(\tau)]$ . In terms of the Wigner function  $W$ , it is given by [97]

$$S(\tau) = 1 - \pi \int d^2\eta W^2(\eta, \tau). \quad (22)$$

We numerically evaluate this equation and provide a graphical representation of each case, as shown in Fig. 8. Across each depicted case, we also carried out a detailed

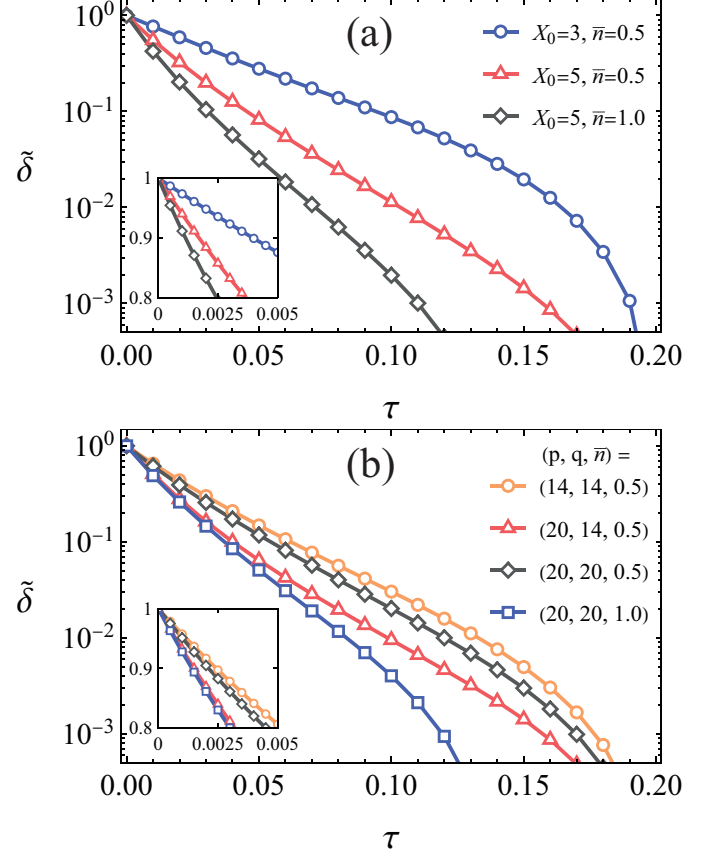


FIG. 7. The temporal evolution of the Wigner negativity of the compass states under the effects of the thermal reservoir: (a)  $p = q = 0$ , and (b)  $X_0 = 1.5$ .

numerical investigation under the variation of the different parameters, which is enclosed in Table I.

When  $\tau = 0$ , the quantum states are pure, indicating that the linear entropy is given by  $S(0) = 0$ . As the coupling of the states with the heat reservoir is significant, the quantum states gradually lose their quantum nature and completely transform into a thermal state. The resulting thermal state  $\hat{\rho}_{\text{th}}$  can be denoted as

$$\hat{\rho}_{\text{th}} = \sum_{m=0}^{\infty} \frac{\bar{n}^m}{(1+\bar{n})^{m+1}} |m\rangle \langle m|, \quad (23)$$

where  $|m\rangle$  represents the eigenstates. At the long time limit ( $\tau \rightarrow \infty$ ), the system reaches the thermal state  $\hat{\rho}_{\text{th}}$ , and the linear entropy approaches a constant value  $S(\tau \rightarrow \infty) = \frac{2\bar{n}}{2\bar{n}+1}$ , which is characteristic of the thermal equilibrium state.

The rate of change of entropy ( $\dot{S}$ ) can be expressed as,

$$\dot{S}(\tau) = \frac{dS}{d\tau}, \quad (24)$$

and after a long interaction ( $\tau \rightarrow \infty$ ) with the heat reservoir, the system reaches thermal equilibrium, a steady state in which the entropy reaches a constant level for

which  $\dot{S}(\tau \rightarrow \infty) = 0$ . However, in contrast to the long-term interaction with the heat reservoir, the change in the purity of the compass states in the vicinity of the  $\tau = 0$  region, denoted as  $S_0 = \dot{S}(0)$ , clearly reflects the impact of decoherence on the states. In other words,  $S_0$  represents the instantaneous rate of change in the entropy, which we evaluate under different parameter choices by analyzing the relative variations in our depicted instances [121].

The relative change in the entropy between two comparable cases is obtained by using

$$\Delta = \left( \frac{S_0^B - S_0^A}{|S_0^A|} \right) \times 100, \quad (25)$$

which quantifies the purity differences between two comparable situations,  $A$  and  $B$ , as an increase (for  $\Delta > 0$ ) or a decrease (for  $\Delta < 0$ ). We provide a graphical representation of multiple situations shown in Fig. 8, followed by a numerical investigation provided in Table I.

Starting with  $p = q = 0$ , depicted in Fig. 8(a), which represents the compass state when  $X_0$  is greater. First, let us check the impact of the amplitude  $X_0$  on the rate of change of entropy, which is observed along the blue and red curves of Fig. 8(a), implying that as  $X_0$  is increased by keeping other parameters constant, the red curve with the higher amplitude  $X_0$  shows a steeper slope near  $\tau = 0$  compared to the blue curve, which is quite apparent at the shorter range of time as shown in the inset of Fig. 8(a). This demonstrates that as the parameter  $X_0$  is increased, the entropy attains a nonzero value more quickly, as evidenced by the rate of change of entropy for the blue curve,  $S_0 = 38.945$ , and for the red curve,  $S_0 = 101.999$ . The numerical results of these two cases are illustrated in Table I along the rows  $i = 1$  and  $i = 2$ , for which the relative rise in the entropy is measured as  $\Delta = 161.90\%$ , implying that in this situation, an increase in the  $X_0$  from  $X_0 = 3$  to  $X_0 = 5$  enhances the loss in purity up to around 161.90%.

An increase in the average thermal photon number of the reservoir leads to a larger change in entropy, as can be observed from the red and black curves in Fig. 8(a). This behavior becomes even clearer when the two curves are compared over a short interval of time, as shown in the inset of Fig. 8(a). The entropy change for the black curve is found to be  $S_0 = 153.999$  ( $i = 3$  in Table I), which is greater than the value for the red curve,  $S_0 = 101.999$  ( $i = 2$  in Table I). These values provide numerical evidence of the stronger increase in entropy as the average photon number increases.

Consider the cases under the change of  $p$ ,  $q$ , and  $\bar{n}$ , while keeping  $X_0$  at a constant lower value, as shown in Fig. 8(b) and their numerical investigation is presented in Table I from  $i = 4$  to  $i = 7$ . First, consider the two comparable cases presented along the rows  $i = 4$  and  $i = 5$  in Table I, where it is shown that increasing the quantity of added photons leads the optimized compass state to lose its purity quickly, which is evident from the

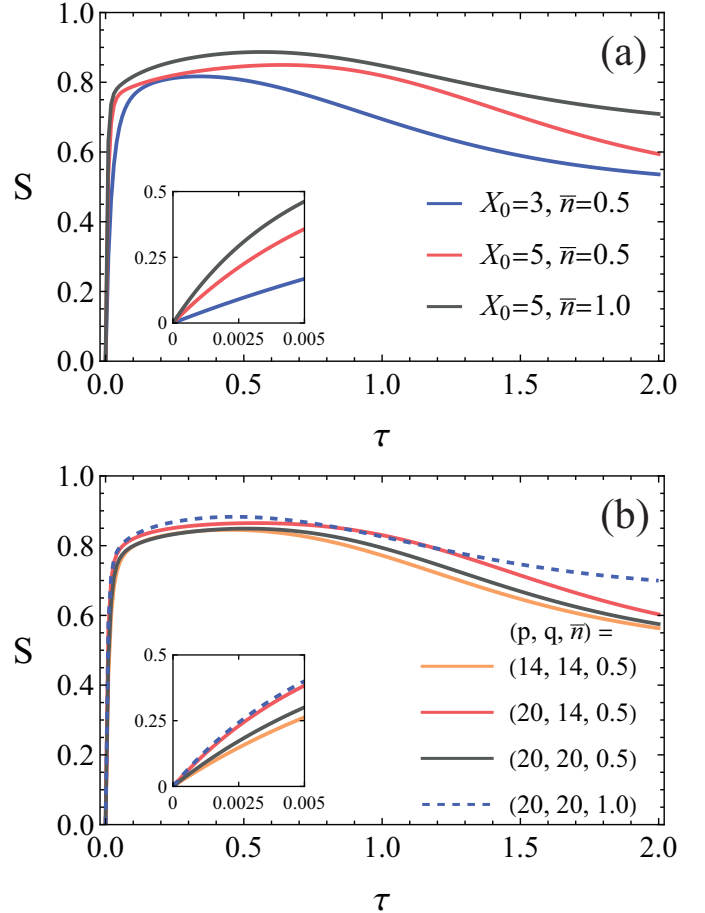


FIG. 8. Linear entropy evolution of the compass states in a thermal reservoir, with insets showing shorter time intervals: (a)  $p = q = 0$ , and (b)  $X_0 = 1.5$ .

orange and red curves with lower and higher photon ( $p$ ) values, respectively. Specifically, for the orange curve,  $S_0 = 66.760$ , while for the red curve  $S_0 = 112.563$ , providing clear numerical evidence for this trend, which further can also be confirmed through the curves provided in the inset of Fig. 8(b) for a relatively short value of  $\tau$  and the relative increase in the linear entropy measured through comparing  $S_0$  for these two cases is  $\Delta = 68.61\%$ .

In contrast to the photon addition, we observe that a higher amount of photon subtraction from the states slows the decay rate of the purity, which is evident in the red and black curves shown in the inset of Fig. 8(b). For the black curve, we evaluate  $S_0 = 79.784$ , which is lower than that of the red curve, indicating that increasing the amount of subtracted photons ( $q$ ) from the optimized compass state decreases the entropy change. These two cases are presented along  $i = 5$  and  $i = 6$  in Table I, implying that increasing photon subtraction ( $q = 14$  to  $q = 20$ ) from the optimized compass state results in a relative drop in entropy change of about  $\Delta = 29.12\%$ .

Finally, the increase in the average thermal photon number (compare  $i = 6$  and  $i = 7$  in Table I) also leads

to a rise in the linear entropy, as both graphically and numerically verified in these instances. This is evident in the comparison between the black and blue curves with lower and higher  $\bar{n}$  values, respectively, which is then clearly visible in the inset of Fig. 8(b). For the blue curve we have  $S_0 = 120.676$ , indicating a greater slope compared to the black curve, which corresponds to a lower value of  $\bar{n}$  and exhibits a slower rate of entropy change, and for this case the relative increase in the entropy while increasing  $\bar{n}$  is  $\Delta = 51.25\%$ .

TABLE I. The data obtained by numerical investigation of the cases presented in Fig. 8.

$i$	$X_0$	$p$	$q$	$\bar{n}$	$S_0$	$\Delta\%$
1	3	0	0	0.5	38.945	$\times$
2	5	0	0	0.5	101.999	161.90
3	5	0	0	1	153.999	50.98
4	1.5	14	14	0.5	66.760	$\times$
5	1.5	20	14	0.5	112.563	68.61
6	1.5	20	20	0.5	79.784	-29.12
7	1.5	20	20	1	120.676	51.25

#### IV. PHASE-SPACE GUIDED DECOHERENCE

In the previous sections, two quantum compass states constructed using different methods were shown to exhibit distinct phase-space characteristics, and their robustness against a thermal reservoir differed accordingly. These observations, supported by multiple theoretical approaches, underscore a strong phase-space dependence in the robustness of quantum states. In this section, we investigate this dependence in a more general framework applicable to any arbitrary pure quantum state.

Let us begin by reformulating Eq. (12) as a partial differential equation in terms of the Wigner function ( $W$ )

$$\begin{aligned} \frac{\partial}{\partial t} W(x, y; t) = & (1 + \bar{n} - \omega \bar{n}) (2W + \boldsymbol{\beta} \cdot \nabla W) \\ & + \frac{1}{2} (1 + \bar{n} + \omega \bar{n}) \nabla \cdot \nabla W. \end{aligned} \quad (26)$$

Recalling that  $\boldsymbol{\beta} = (x, y)^\top$  represents the radius vector in phase space and  $\nabla = \left(\frac{\partial}{\partial x}, \frac{\partial}{\partial y}\right)$  denotes the phase space divergence operator, defined with respect to the position coordinate  $x$  and the momentum coordinate  $y$ . The corresponding equation takes the form of the famous Fokker–Planck equation, with the two terms on the right-hand side of Eq. (26) illustrating distinct and intuitive physical interpretations.

The first term of Eq. (26) governs the contraction of structures in phase space, accompanied by an increase

in the amplitude of the Wigner function; however, this process alone neither diminishes nor enhances the negativity of the Wigner function ( $\delta$ ) defined in Eq. (21). The second term of Eq. (26) corresponds to a diffusion process analogous to the well-known heat equation, through which the Wigner function redistributes from regions of higher amplitude to those of lower amplitude. As a result, the negativity of the Wigner function is gradually suppressed, leading to the eventual disappearance of non-classical features.

We now investigate the impact of decoherence from the heat reservoir on the nonclassical characteristics of a quantum state. To do so, we first quantitatively analyze the effects on a phase-space structure by examining the instantaneous rate of change along a selective volume in the Wigner phase space. We consider a time-dependent patch  $A(\tau)$  with boundary  $\partial A(\tau)$ . The volume of the Wigner function over this patch is defined as  $v(\tau)$ , and thus the rate of change of  $v(\tau)$  is defined as

$$\dot{v}(\tau) = \frac{dv(\tau)}{d\tau} = \iint_{A(\tau)} \frac{\partial W(\tau)}{\partial \tau} dx dy, \quad (27)$$

when the Wigner function within the patch is positive,  $v(\tau) > 0$ ; when it is negative,  $v(\tau) < 0$ . By applying the Reynolds transport theorem [122], we obtain

$$\dot{v}(\tau) = \left( \bar{n} + \frac{1}{2} \right) \oint_{\partial A(\tau)} \nabla W(x, y; \tau) \cdot \mathbf{n} dl, \quad (28)$$

where  $\mathbf{n}$  is the outward-pointing normal vector of the boundary  $\partial A(\tau)$ . Since the signs of  $v(\tau)$  and any  $\nabla W(x, y; \tau) \cdot \mathbf{n}$  on the boundary  $\partial A(\tau)$  must be opposite, the tiny-scale structures in phase space are inevitably prone to disruption.

Apart from volume loss, we now examine the variation in the impact of decoherence across phase-space patches at the different scales (or areas), which can be characterized by tracking the motion of the zero points of the associated Wigner functions. Consider a simply connected region labeled as  $A(\tau)$  with boundary  $\partial A(\tau)$ . The time evolution of the area  $a_{\pm}(\tau)$  of this region is given as follows,

$$\dot{a}_{\pm}(\tau) = \frac{da_{\pm}(\tau)}{d\tau} = \frac{d}{d\tau} \iint_{A(\tau)} dx dy = \int_{\partial A(\tau)} \mathbf{v}_b \cdot \mathbf{n} dl, \quad (29)$$

where the subscript of  $a_{\pm}$  indicates whether the patch is positively (+) or negatively peaked (-),  $\mathbf{v}_b$  is the Eulerian velocity of the boundary, which should not be confused with the velocity field associated with the Wigner function [123].

The boundary conditions  $W(x(\tau), y(\tau); \tau) = 0$  in the Lagrangian description lead to

$$\frac{dW}{d\tau} = \frac{\partial}{\partial \tau} W + \left( \frac{\partial}{\partial \tau} \boldsymbol{\beta} \right) \cdot \nabla W = 0, \quad (30)$$

and with the Lagrangian and Eulerian specifications of the flow field, which are related as  $\mathbf{v}_b = \frac{\partial \boldsymbol{\beta}}{\partial \tau}$ . Equation

(29) is rewritten as follows:

$$\begin{aligned}\dot{a}_{\pm}(\tau) &= -2a_{\pm}(\tau) \pm \left(\bar{n} + \frac{1}{2}\right) \oint_{\partial A(\tau)} \frac{\nabla \cdot \nabla W}{|\nabla W|} dl \\ &= -2a_{\pm}(\tau) - 2\pi \left(\bar{n} + \frac{1}{2}\right) \\ &\quad - \left(\bar{n} + \frac{1}{2}\right) \oint_{\partial A(\tau)} \nabla (\ln|\nabla W|) \cdot \mathbf{n} dl.\end{aligned}\quad (31)$$

Here,  $-2a_{\pm}(\tau)$  arises from a term associated with the contraction of the phase space pattern in the Eq. (26), while  $-2\pi(\bar{n} + \frac{1}{2})$  represents a geometric effect [124] independent of the specific shape of the boundary  $\partial A(\tau)$ .

TABLE II. The data obtained through the numerical integration of Eqs. (28) and (31) for the specific instances of the compass state and its optimized version, as considered in our work.

$i$	$X_0$	$p$	$q$	$a_+(0)$	$v(0)$	$\dot{v}(0)$	$\frac{\dot{v}(0)}{v(0)}$	$\dot{a}_+(0)$
1	3	0	0	0.503	0.129	-4.52	-35.0	1.68
2	5	0	0	0.197	0.0500	-4.80	-96.1	1.18
3	1.5	14	14	0.274	0.0739	-4.88	-65.9	0.0918
4	1.5	20	20	0.234	0.0624	-4.87	-78.1	0.300
5	1.5	20	14	0.163	0.0441	-4.96	-112	-0.0545

In a special case, if the patch  $A(\tau)$  under examination is a circular-shaped region with a radius  $r$  and the Wigner function has rotational symmetry along its boundary. The coordinate system centered at the origin, defined as the center of the circle, has a simple form;

$$\dot{a}_{\pm}(\tau) \simeq -2a_{\pm}(\tau) - 2\pi \left(\bar{n} + \frac{1}{2}\right) \left(1 + r \frac{W''(r)}{W'(r)}\right). \quad (32)$$

In Table II, we analyze the decay of the central crucial phase-space feature of the associated compass state and its optimized variant. We computed the area  $a_+(0)$  of the central patch (among all the enumerated examples, the considered patches are positively peaked) and the volume of the Wigner function  $v(0)$  over the patch, as well as the instantaneous rates of change of both the area  $\dot{a}_+(0)$  and the volume  $\dot{v}(0)$ , evaluated at an average thermal photon number kept constant to  $\bar{n} = 0.5$ .

From Table II, the relative instantaneous reduction in the area denoted as  $\dot{a}_+(0)$  and the relative reduction in the volume measured through  $\frac{\dot{v}(0)}{v(0)}$  highlight the decreases across different initial patches of areas  $a_+(0)$  and volumes  $v(0)$  in the presence of thermal decoherence. These results show that patches at lower scales tend to lose their existence more quickly. This behavior is further corroborated by our analysis in the previous section, where it is justified with different theoretical frameworks. In summary, it is observed that a reduction in the size of the smallest central phase-space features leads to an

enhanced susceptibility to decoherence, suggesting that quantum states at these finer scales are more vulnerable to decoherence.

## V. SUMMARY

We considered the compass state and its variant obtained by applying photon addition and then subtraction operations, and both of these two states provide a variety of phase-space features with comparatively larger extensions to the tiny features at the sub-Planckian scale, as well as a fair comparison of the varying effects of decoherence analyzed through these varieties of phase-space features. Our first indication is that a properly generated photon-added and subtracted variant of the compass state can yield an isotropic form of the sub-Planck structures in the same fashion as its counter variant introduced in the previous work [43]. The current variant of the compass state was overlooked to exhibit isotropy in its phase-space sub-Planckian traits and sensitivity to perturbations, a positive outcome for quantum sensing. We thoroughly focused on the impact of decoherence arising from a heat bath on these two compass states, supported by the number of theoretical techniques resulting in unified results.

Another exclusive aspect of our work is the establishment of a connection between the effects of decoherence and the spatial sizes or extents of the phase-space structures associated with the outlined compass states. Additionally, our results are generalizable to any arbitrary pure quantum state interacting with the considered heat reservoir. Our findings indicate that quantum states with finer phase-space structures are more prone to decoherence. In the examples we examined, adding photons to superposition states, or increasing the amplitudes of the corresponding superposed coherent states, results in progressively delicate phase-space features, making the states more fragile. Photon subtraction produces the opposite effect. Small-scale structures degrade faster than those occupying larger regions of phase space, highlighting the limited robustness of crucial sub-Planckian structures when decoherence is present.

## ACKNOWLEDGEMENT

This work was supported by the National Natural Science Foundation of China (Grants No. 12475009, No. 12075001, and No. 61601002), the Anhui Provincial Key Research and Development Plan (Grant No. 2022b13020004), the Anhui Province Science and Technology Innovation Project (Grant No. 202423r06050004), the Anhui Provincial Department of Industry and Information Technology (Grant No. JB24044), the Anhui Province Natural Science Foundation (Grant No. 202508140141), and the Anhui Provincial University Scientific Research Major

Project (Grant No. 2024AH040008). Jia-Xin Peng acknowledges the support from the National Natural Science Foundation of China (Grant No. 12504566), the Natural Science Foundation of Jiangsu Province (Grant

No. BK20250947), the Natural Science Foundation of the Jiangsu Higher Education Institutions (Grant No. 25KJB140013), and the Natural Science Foundation of Nantong City (Grant No. JC2024045).

---

[1] C. Gerry and P. Knight, *Introductory Quantum Optics* (Cambridge University Press, England, Cambridge, 2005).

[2] Z. Ficek and S. Swain, *Quantum Interference and Coherence: Theory and Experiments*, Vol. 100 (Springer Science & Business Media, Berlin, Germany, 2005).

[3] M. Malnou, D. A. Palken, B. M. Brubaker, L. R. Vale, G. C. Hilton, and K. W. Lehnert, Squeezed vacuum used to accelerate the search for a weak classical signal, *Physical Review X* **9**, 021023 (2019).

[4] W. J. Munro, K. Nemoto, G. J. Milburn, and S. L. Braunstein, Weak-force detection with superposed coherent states, *Physical Review A* **66**, 023819 (2002).

[5] P. Walther, J.-W. Pan, M. Aspelmeyer, R. Ursin, S. Gasparoni, and A. Zeilinger, De Broglie wavelength of a non-local four-photon state, *Nature* **429**, 158 (2004).

[6] M. W. Mitchell, J. S. Lundeen, and A. M. Steinberg, Super-resolving phase measurements with a multiphoton entangled state, *Nature* **429**, 161 (2004).

[7] H. Kwon, K. C. Tan, T. Volkoff, and H. Jeong, Nonclassicality as a quantifiable resource for quantum metrology, *Physical Review Letters* **122**, 040503 (2019).

[8] W. Ge, K. Jacobs, S. Asiri, M. Foss-Feig, and M. S. Zubairy, Operational resource theory of nonclassicality via quantum metrology, *Physical Review Research* **2**, 023400 (2020).

[9] H. Jeong, M. S. Kim, and J. Lee, Quantum-information processing for a coherent superposition state via a mixed-entangled coherent channel, *Physical Review A* **64**, 052308 (2001).

[10] F. Fröwis, P. Sekatski, W. Dür, N. Gisin, and N. Sangouard, Macroscopic quantum states: Measures, fragility, and implementations, *Rev. Mod. Phys.* **90**, 025004 (2018).

[11] C. Fabre and N. Treps, Modes and states in quantum optics, *Rev. Mod. Phys.* **92**, 035005 (2020).

[12] G. J. Milburn, Quantum and classical Liouville dynamics of the anharmonic oscillator, *Physical Review A* **33**, 674 (1986).

[13] B. Yurke and D. Stoler, Generating Quantum Mechanical Superpositions of Macroscopically Distinguishable States via Amplitude Dispersion, *Physical Review Letters* **57**, 13 (1986).

[14] J. Liu, W. Ge, and M. S. Zubairy, Classical-nonclassical polarity of Gaussian states, *Phys. Rev. Lett.* **132**, 240201 (2024).

[15] D. Kienzler, C. Flühmann, V. Negnevitsky, H.-Y. Lo, M. Marinelli, D. Nadlinger, and J. P. Home, Observation of quantum interference between separated mechanical oscillator wave packets, *Physical Review Letters* **116**, 140402 (2016).

[16] C. Navarrete-Benlloch, *An Introduction to the Formalism of Quantum Information with Continuous Variables* (Morgan & Claypool/IOP, Bristol, 2015).

[17] W. P. Schleich, *Quantum Optics in Phase Space* (Wiley-VCH, Weinheim, 2001).

[18] J. Davis, M. Kumari, R. B. Mann, and S. Ghose, Wigner negativity in spin- $j$  systems, *Physical Review Research* **3**, 033134 (2021).

[19] U. Chabaud, P.-E. Emeriau, and F. Grosshans, Witnessing Wigner Negativity, *Quantum* **5**, 471 (2021).

[20] N. Delfosse, P. Allard Guerin, J. Bian, and R. Raussendorf, Wigner function negativity and contextuality in quantum computation on Rebits, *Physical Review X* **5**, 021003 (2015).

[21] H. P. Robertson, The uncertainty principle, *Physical Review* **34**, 163 (1929).

[22] W. H. Zurek, Sub-Planck structure in phase space and its relevance for quantum decoherence, *Nature* **412**, 712 (2001).

[23] L. A. Howard, T. J. Weinhold, F. Shahandeh, J. Combes, M. R. Vanner, A. G. White, and M. Ringbauer, Quantum hypercube states, *Physical Review Letters* **123**, 020402 (2019).

[24] P. Zheng, Y. Cai, B. Xu, S. Wen, L. Zhang, Z. Ni, J. Mai, Y. Zeng, L. Lin, L. Hu, X. Deng, S. Liu, J. Shu, Y. Xu, and D. Yu, Quantum-enhanced dark matter detection using Schrödinger cat states (2025), arXiv:2507.23538 [quant-ph].

[25] D. A. R. Dalvit, R. L. de Matos Filho, and F. Toscano, Quantum metrology at the Heisenberg limit with ion trap motional compass states, *New Journal of Physics* **8**, 276 (2006).

[26] F. Toscano, D. A. R. Dalvit, L. Davidovich, and W. H. Zurek, Sub-Planck phase-space structures and Heisenberg-limited measurements, *Physical Review A* **73**, 023803 (2006).

[27] X. Deng, S. Li, Z.-J. Chen, Z. Ni, Y. Cai, J. Mai, L. Zhang, P. Zheng, H. Yu, C.-L. Zou, and et al., Quantum-enhanced metrology with large Fock states, *Nature Physics* , 1 (2024).

[28] K. Park, P. Marek, U. L. Andersen, and R. Filip, Quantum Rabi interferometry of motion and radiation, *Quantum* **7**, 1024 (2023).

[29] K. Jacobs, P. L. Knight, and V. Vedral, Determining the state of a single cavity mode from photon statistics, in *Quantum Electronics and Laser Science Conference* (Optica Publishing Group, 1997) p. QWD17.

[30] Y.-R. Chen, H.-Y. Hsieh, J. Ning, H.-C. Wu, H. L. Chen, Z.-H. Shi, P. Yang, O. Steuernagel, C.-M. Wu, and R.-K. Lee, Generation of heralded optical cat states by photon addition, *Physical Review A* **110**, 023703 (2024).

[31] J. Wenger, R. Tualle-Brouri, and P. Grangier, Non-Gaussian statistics from individual pulses of squeezed light, *Physical Review Letters* **92**, 153601 (2004).

[32] M. Dakna, T. Anhut, T. Opatrný, L. Knöll, and D.-G. Welsch, Generating Schrödinger-cat-like states by means of conditional measurements on a beam splitter,

Physical Review A **55**, 3184 (1997).

[33] X.-B. Tang, F. Gao, Y.-X. Wang, J.-G. Wu, and F. Shuang, Non-Gaussian features from excited squeezed vacuum state, *Optics Communications* **345**, 86 (2015).

[34] S. M. Barnett, G. Ferenczi, C. R. Gilson, and F. C. Speirs, Statistics of photon-subtracted and photon-added states, *Physical Review A* **98**, 013809 (2018).

[35] S. Guerrini, M. Z. Win, and A. Conti, Photon-varied quantum states: Unified characterization, *Physical Review A* **108**, 022425 (2023).

[36] A. Zavatta, V. Parigi, M. S. Kim, and M. Bellini, Subtracting photons from arbitrary light fields: experimental test of coherent state invariance by single-photon annihilation, *New Journal of Physics* **10**, 123006 (2008).

[37] M. M. Lund, F. Yang, V. R. Christiansen, D. Kornovan, and K. Mølmer, Subtraction and addition of propagating photons by two-level emitters, *Physical Review Letters* **133**, 103601 (2024).

[38] K. Takase, J.-i. Yoshikawa, W. Asavanant, M. Endo, and A. Furusawa, Generation of optical Schrödinger cat states by generalized photon subtraction, *Physical Review A* **103**, 013710 (2021).

[39] A. Hertz, N. J. Cerf, and S. De Bièvre, Relating the entanglement and optical nonclassicality of multimode states of a bosonic quantum field, *Physical Review A* **102**, 032413 (2020).

[40] N. Akhtar, J. Wu, J.-X. Peng, W.-M. Liu, and G. Xianlong, Sub-Planck structures and sensitivity of the superposed photon-added or photon-subtracted squeezed-vacuum states, *Physical Review A* **107**, 052614 (2023).

[41] A. Ourjoumtsev, R. Tualle-Brouri, J. Laurat, and P. Grangier, Generating optical Schrödinger kittens for quantum information processing, *Science* **312**, 83 (2006).

[42] J. S. Neergaard-Nielsen, B. M. Nielsen, C. Hettich, K. Mølmer, and E. S. Polzik, Generation of a Superposition of Odd Photon Number States for Quantum Information Networks, *Physical Review Letters* **97**, 083604 (2006).

[43] N. Akhtar, X. Yang, J.-X. Peng, I. Ul Haq, Y. Xie, and Y. Chen, Sub-shot-noise sensitivity via superpositions of two deformed kitten states, *Physical Review A* **111**, 032407 (2025).

[44] D. C. Brody, E.-M. Graefe, and R. Melanathuru, Phase-space measurements, decoherence, and classicality, *Phys. Rev. Lett.* **134**, 120201 (2025).

[45] J. Twamley, Phase-space decoherence: A comparison between consistent histories and environment-induced superselection, *Physical Review D* **48**, 5730 (1993).

[46] K. Tsubouchi, Y. Mitsuhashi, R. Takagi, and N. Yoshioka, Symmetric channel verification for purifying noisy quantum channels, *PRX Quantum* **6**, 040310 (2025).

[47] A. Ullah, T. M. Naseem, and O. E. Müstecapoglu, Mixing thermal coherent states for precision and range enhancement in quantum thermometry, *Quantum Science and Technology* **10**, 015044 (2024).

[48] D. Braun, F. Haake, and W. T. Strunz, Universality of decoherence, *Physical Review Letters* **86**, 2913 (2001).

[49] J. C. Retamal and N. Zagury, Stability of quantum states under dissipation, *Physical Review A* **63**, 032106 (2001).

[50] T. Pellizzari, S. A. Gardiner, J. I. Cirac, and P. Zoller, Decoherence, continuous observation, and quantum computing: A cavity QED model, *Physical Review Letters* **75**, 3788 (1995).

[51] M. Schlosshauer, Quantum decoherence, *Physics Reports* **831**, 1 (2019).

[52] W. H. Zurek, Decoherence, einselection, and the quantum origins of the classical, *Reviews of Modern Physics* **75**, 715 (2003).

[53] W. H. Zurek, Decoherence and the transition from quantum to classical, *Physics today* **44**, 36 (1991).

[54] K. Modi, A. Brodutch, H. Cable, T. Paterek, and V. Vedral, The classical-quantum boundary for correlations: Discord and related measures, *Reviews of Modern Physics* **84**, 1655 (2012).

[55] C. Gardiner and P. Zoller, *Quantum Noise 2nd Edition* (Springer, Berlin Heidelberg, 1999).

[56] P. W. Shor, Scheme for reducing decoherence in quantum computer memory, *Physical Review A* **52**, R2493 (1995).

[57] F. Fröwis, P. Sekatski, W. Dür, N. Gisin, and N. Sangouard, Macroscopic quantum states: Measures, fragility, and implementations, *Reviews of Modern Physics* **90**, 025004 (2018).

[58] M. S. Kim and V. Bužek, Schrödinger-cat states at finite temperature: Influence of a finite-temperature heat bath on quantum interferences, *Physical Review A* **46**, 4239 (1992).

[59] N. Akhtar, X. Yang, M. Asjad, J.-X. Peng, G. Xianlong, and Y. Chen, Compasslike states in a thermal reservoir and fragility of their nonclassical features, *Physical Review A* **109**, 053718 (2024).

[60] B. D. Hauer, J. Combes, and J. D. Teufel, Nonlinear sideband cooling to a cat state of motion, *Physical Review Letters* **130**, 213604 (2023).

[61] C. J. Myatt, B. E. King, Q. A. Turchette, C. A. Sackett, D. Kielpinski, W. M. Itano, C. Monroe, and D. J. Wineland, Decoherence of quantum superpositions through coupling to engineered reservoirs, *Nature* **403**, 269 (2000).

[62] S. Deleglise, I. Dotsenko, C. Sayrin, J. Bernu, M. Brune, J.-M. Raimond, and S. Haroche, Reconstruction of nonclassical cavity field states with snapshots of their decoherence, *Nature* **455**, 510 (2008).

[63] M. Brune, E. Hagley, J. Dreyer, X. Maître, A. Maali, C. Wunderlich, J. M. Raimond, and S. Haroche, Observing the progressive decoherence of the “Meter” in a quantum measurement, *Physical Review Letters* **77**, 4887 (1996).

[64] F.-X. Sun, Y. Fang, Q. He, and Y. Liu, Generating optical cat states via quantum interference of multi-path free-electron–photons interactions, *Science Bulletin* **68**, 1366 (2023).

[65] M. Kolář and R. Filip, Negative Wigner function by decaying interaction from equilibrium, *Quantum* **8**, 1566 (2024).

[66] G. S. Agarwal, Brownian motion of a quantum oscillator, *Physical Review A* **4**, 739 (1971).

[67] C. Monroe, D. M. Meekhof, B. E. King, and D. J. Wineland, A “Schrödinger cat” superposition state of an atom, *Science* **272**, 1131 (1996).

[68] Q. A. Turchette, C. S. Wood, B. E. King, C. J. Myatt, D. Leibfried, W. M. Itano, C. Monroe, and D. J. Wineland, Deterministic entanglement of two trapped ions, *Physical Review Letters* **81**, 3631 (1998).

[69] J. F. Poyatos, J. I. Cirac, and P. Zoller, Quantum reservoir engineering with laser cooled trapped ions, *Physical Review Letters* **77**, 4728 (1996).

[70] A. J. Leggett, S. Chakravarty, A. T. Dorsey, M. P. A. Fisher, A. Garg, and W. Zwerger, Dynamics of the dissipative two-state system, *Reviews of Modern Physics* **59**, 1 (1987).

[71] A. J. Leggett, S. Chakravarty, A. T. Dorsey, M. P. A. Fisher, A. Garg, and W. Zwerger, Erratum: Dynamics of the dissipative two-state system, *Reviews of Modern Physics* **67**, 725 (1995).

[72] A. L. A.O Caldeira, Quantum tunnelling in a dissipative system, *Annals of Physics* **149**, 374 (1983).

[73] A. Caldeira and A. Leggett, Path integral approach to quantum Brownian motion, *Physica A: Statistical Mechanics and its Applications* **121**, 587 (1983).

[74] A. O. Caldeira and A. J. Leggett, Influence of damping on quantum interference: An exactly soluble model, *Physical Review A* **31**, 1059 (1985).

[75] A. J. Leggett, Schrödinger's cat and her laboratory cousins, *Contemporary Physics* **25**, 583 (1984).

[76] C. Sackett, C. Monroe, and D. Wineland, Decoherence of motional superpositions of a trapped ion, *Chaos, Solitons & Fractals* **16**, 431 (2003).

[77] D. F. Walls and G. J. Milburn, Effect of dissipation on quantum coherence, *Physical Review A* **31**, 2403 (1985).

[78] H. Jeong and T. C. Ralph, Quantum superpositions and entanglement of thermal states at high temperatures and their applications to quantum-information processing, *Physical Review A* **76**, 042103 (2007).

[79] W. Schleich and J. A. Wheeler, Oscillations in photon distribution of squeezed states and interference in phase space, *Nature* **326**, 574 (1987).

[80] X. Yu, B. Wilhelm, D. Holmes, A. Vaartjes, D. Schwienbacher, M. Nurizzo, A. Kringshøj, M. R. v. Blankenstein, A. M. Jakob, P. Gupta, *et al.*, Schrödinger cat states of a nuclear spin qudit in silicon, *Nature Physics* **1**, 1 (2025).

[81] I. Yang, T. Agrenius, V. Usova, O. Romero-Isart, and G. Kirchmair, Hot Schrödinger cat states, *Science Advances* **11**, eadrr4492 (2025).

[82] H. Takahashi, K. Wakui, S. Suzuki, M. Takeoka, K. Hayasaka, A. Furusawa, and M. Sasaki, Generation of large-amplitude coherent-state superposition via Ancilla-Assisted photon subtraction, *Physical Review Letters* **101**, 233605 (2008).

[83] A. Ourjoumtsev, H. Jeong, R. Tualle-Brouri, and P. Grangier, Generation of optical 'Schrödinger cats' from photon number states, *Nature* **448**, 784 (2007).

[84] J. Etesse, M. Bouillard, B. Kanseri, and R. Tualle-Brouri, Experimental generation of squeezed cat states with an operation allowing iterative growth, *Physical Review Letters* **114**, 193602 (2015).

[85] K. Huang, H. Le Jeannic, J. Ruaudel, V. B. Verma, M. D. Shaw, F. Marsili, S. W. Nam, E. Wu, H. Zeng, Y.-C. Jeong, R. Filip, O. Morin, and J. Laurat, Optical synthesis of large-amplitude squeezed coherent-state superpositions with minimal resources, *Physical Review Letters* **115**, 023602 (2015).

[86] B. Vlastakis, G. Kirchmair, Z. Leghtas, S. E. Nigg, L. Frunzio, S. M. Girvin, M. Mirrahimi, M. H. Devoret, and R. J. Schoelkopf, Deterministically encoding quantum information using 100-photon Schrödinger cat states, *Science* **342**, 607 (2013).

[87] C. Monroe, D. M. Meekhof, B. E. King, and D. J. Wineland, A "Schrödinger cat" superposition state of an atom, *Science* **272**, 1131 (1996).

[88] H.-Y. Lo, D. Kienzler, L. de Clercq, M. Marinelli, V. Negnevitsky, B. C. Keitch, and J. P. Home, Spin-motion entanglement and state diagnosis with squeezed oscillator wavepackets, *Nature* **521**, 336 (2015).

[89] D. Vitali, P. Tombesi, and G. J. Milburn, Quantum-state protection in cavities, *Physical Review A* **57**, 4930 (1998).

[90] H. Le Jeannic, A. Cavaillès, K. Huang, R. Filip, and J. Laurat, Slowing quantum decoherence by squeezing in phase space, *Physical Review Letters* **120**, 073603 (2018).

[91] X. Pan, J. Schwinger, N.-N. Huang, P. Song, W. Chua, F. Hanamura, A. Joshi, F. Valadares, R. Filip, and Y. Y. Gao, Protecting the quantum interference of cat states by phase-space compression, *Physical Review X* **13**, 021004 (2023).

[92] K. Berrada and H. Eleuch, Noncommutative deformed cat states under decoherence, *Physical Review D* **100**, 016020 (2019).

[93] D.-W. Liu, Y. Wu, and L.-G. Si, Magnon cat states induced by photon parametric coupling, *Physical Review Applied* **21**, 044018 (2024).

[94] R. Y. Teh, P. D. Drummond, and M. D. Reid, Overcoming decoherence of Schrödinger cat states formed in a cavity using squeezed-state inputs, *Physical Review Research* **2**, 043387 (2020).

[95] D. Viennot, Competition between decoherence and purification: Quaternionic representation and quaternionic fractals, *Chaos, Solitons & Fractals* **161**, 112346 (2022).

[96] J. Schneeloch, C. C. Tison, H. S. Jacinto, and P. M. Alsing, Negativity vs. purity and entropy in witnessing entanglement, *Scientific Reports* **13**, 4601 (2023).

[97] J. S. Sales and N. G. de Almeida, Robustness of superposition states evolving under the influence of a thermal reservoir, *Physical Review A* **83**, 062121 (2011).

[98] A. Kenfack and K. Życzkowski, Negativity of the Wigner function as an indicator of non-classicality, *Journal of Optics B: Quantum and Semiclassical Optics* **6**, 396 (2004).

[99] U. Leonhardt, Quantum-state tomography and discrete Wigner function, *Physical Review Letters* **74**, 4101 (1995).

[100] U. Leonhardt, Discrete Wigner function and quantum-state tomography, *Physical Review A* **53**, 2998 (1996).

[101] K. Vogel and H. Risken, Determination of quasiprobability distributions in terms of probability distributions for the rotated quadrature phase, *Physical Review A* **40**, 2847 (1989).

[102] I. Strandberg, Simple, reliable, and noise-resilient continuous-variable quantum state tomography with convex optimization, *Physical Review Applied* **18**, 044041 (2022).

[103] P. Jacquod, I. Adagideli, and C. W. J. Beenakker, Decay of the Loschmidt Echo for Quantum States with Sub-Planck-scale Structures, *Physical Review Letters* **89**, 154103 (2002).

[104] S. Ghosh, A. Chiruvelli, J. Banerji, and P. K. Panigrahi, Mesoscopic superposition and sub-Planck-scale structure in molecular wave packets, *Physical Review*

**A** **73**, 013411 (2006).

[105] M. Stobińska, G. J. Milburn, and K. Wódkiewicz, Wigner function evolution of quantum states in the presence of self-Kerr interaction, *Physical Review A* **78**, 013810 (2008).

[106] S. Ghosh, U. Roy, C. Genes, and D. Vitali, Sub-Planck-scale structures in a vibrating molecule in the presence of decoherence, *Physical Review A* **79**, 052104 (2009).

[107] U. Roy, S. Ghosh, P. K. Panigrahi, and D. Vitali, Sub-Planck-scale structures in the Pöschl-teller potential and their sensitivity to perturbations, *Physical Review A* **80**, 052115 (2009).

[108] N. Akhtar, B. C. Sanders, and C. Navarrete-Benlloch, Sub-Planck structures: Analogies between the Heisenberg-Weyl and SU(2) groups, *Physical Review A* **103**, 053711 (2021).

[109] N. Akhtar, B. C. Sanders, and G. Xianlong, Sub-Planck phase-space structure and sensitivity for SU(1,1) compass states, *Physical Review A* **106**, 043704 (2022).

[110] S. Luo, S. Tang, and Y. Zhang, Optimal circular states, *Journal of Physics A: Mathematical and Theoretical* **57**, 465301 (2024).

[111] T. Hailin, N. Akhtar, and G. Xianlong, Multicomponent cat states with sub-Planckian structures and their optomechanical analogues, *Physical Review Applied* **24**, 024053 (2025).

[112] A. Kenfack and K. Życzkowski, Negativity of the Wigner function as an indicator of non-classicality, *Journal of Optics B: Quantum and Semiclassical Optics* **6**, 396 (2004).

[113] N. Shukla, N. Akhtar, and B. C. Sanders, Quantum tetrachotomous states: Superposition of four coherent states on a line in phase space, *Physical Review A* **99**, 063813 (2019).

[114] R. P. Rundle and M. J. Everitt, Overview of the phase space formulation of quantum mechanics with application to quantum technologies, *Advanced Quantum Technologies* **4**, 2100016 (2021).

[115] A. Shukla and B. C. Sanders, Superposing compass states for asymptotic isotropic sub-Planck phase-space sensitivity, *Physical Review A* **108**, 043719 (2023).

[116] V. Bužek, A. Vidiella-Barranco, and P. L. Knight, Superpositions of coherent states: Squeezing and dissipation, *Physical Review A* **45**, 6570 (1992).

[117] L.-y. Hu and H.-y. Fan, Time evolution of Wigner function in laser process derived by entangled state representation, *Optics Communications* **282**, 4379 (2009).

[118] F. Hong-Yi and F. Yue, New bosonic operator ordering identities gained by the entangled state representation and two-variable Hermite polynomials\*, *Communications in Theoretical Physics* **38**, 297 (2002).

[119] X.-G. Meng, K.-C. Li, J.-S. Wang, Z.-S. Yang, X.-Y. Zhang, Z.-T. Zhang, and B.-L. Liang, Multi-variable special polynomials using an operator ordering method, *Frontiers of Physics* **15**, 1.

[120] R. R. Puri, *Mathematical Methods of Quantum Optics* (Springer-Verlag, Berlin, 2001).

[121] Y. O. Vartiainen, *Relative Changes and Index Numbers* (The Research Institute of the Finnish Economy, Helsinki, 1976).

[122] W. Dittrich and M. Reuter, *Classical and Quantum Dynamics: From Classical Paths to Path Integrals* (Springer, Berlin, 1996).

[123] M. Oliva, D. Kakofengitis, and O. Steuernagel, Anharmonic quantum mechanical systems do not feature phase space trajectories, *Physica A: Statistical Mechanics and its Applications* **502**, 201 (2018).

[124] R. Goldman, Curvature formulas for implicit curves and surfaces, *Computer Aided Geometric Design* **22**, 632 (2005).